Nanocrystalline Nd_2Fe_{17} synthesized by high-energy ball milling: crystal structure, microstructure and magnetic properties

2010 J. Phys.: Condens. Matter 22 216005

(http://iopscience.iop.org/0953-8984/22/21/216005)

J. Phys.: Condens. Matter **22** (2010) 216005 (8pp) doi:10.1088/0953-8984/22/21/216005

Nanocrystalline Nd_2Fe_{17} synthesized by high-energy ball milling: crystal structure, microstructure and magnetic properties

Pablo Álvarez[1], Pedro Gorria[1], Victorino Franco[2], Jorge Sánchez Marcos[3], María J Pérez[1], José L Sánchez Llamazares[1], Inés Puente Orench[4,5] and Jesús A Blanco[1]

[1] Departamento de Física, Universidad de Oviedo, Calvo Sotelo, s/n, 33007 Oviedo, Spain
[2] Departamento Física de la Materia Condensada, ICMSE-CSIC, Universidad de Sevilla, PO Box 1065, 41080 Sevilla, Spain
[3] Instituto de Ciencia de Materiales de Madrid, CSIC, Cantoblanco, 28049 Madrid, Spain
[4] Institute Laue-Langevin, BP 156, 6 rue Jules Horowitz, 38042 Grenoble Cedex 9, France
[5] Instituto de Ciencia de Materiales de Aragón, CSIC—Universidad de Zaragoza, 50009 Zaragoza, Spain

E-mail: alvarezpablo.uo@uniovi.es

Received 22 December 2009, in final form 23 March 2010
Published 5 May 2010
Online at stacks.iop.org/JPhysCM/22/216005

Abstract

Nanocrystalline Nd_2Fe_{17} powders have been obtained by means of high-energy ball milling from nearly single-phase bulk alloys produced by arc melting and high temperature homogenization annealing. The rhombohedral Th_2Zn_{17}-type crystal structure of the bulk alloy remains unaltered after the milling process, with almost unchanged values for the cell parameters. However, the severe mechanical processing induces drastic microstructural changes. A decrease of the mean crystalline size down to around 10 nm is observed, giving rise to a considerable augmentation of the disordered inter-grain boundaries. This modification of the microstructure affects the magnetic behaviour of the milled powders, although the magnetic structure remains collinear ferromagnetic. While a unique ferro-to-paramagnetic transition temperature, $T_C = 339 \pm 2$ K, is observed in the bulk alloy, the nanocrystalline samples exhibit a more likely distribution of T_C values. The latter seems to be responsible for the significant broadening of the temperature range in which magneto-caloric effect is observed, and the lowering of the maximum value of the magnetic entropy change.

(Some figures in this article are in colour only in the electronic version)

1. Introduction

High-energy ball milling (HEBM) is a widely used technique for the mechanical alloying or processing of a great variety of materials [1–3], and has opened exciting horizons in the production of materials with *sui-generis* and enhanced properties for different technological purposes. This technique allows the synthesis of diverse iron-based metallic metastable materials far from the thermodynamical equilibrium, such as amorphous metallic glasses [4–6] or disordered and supersaturated solid solutions [7–10]. Moreover, the microstructure of bulk alloys, obtained by other conventional fabrication routes, can be largely modified by means of severe mechanical processing using HEBM, giving rise in most cases to drastic changes in their physico-chemical behaviour [11–15]. In this way, HEBM permits obtaining nanocrystalline alloys with mean crystallite size even below 10 nm [16, 17].

R–Fe (R = rare earth) intermetallic compounds display a great variety of crystalline structures and different magnetic behaviours depending on the stoichiometry and the nature of the R ion [18, 19]. These alloys are therefore

attractive from a fundamental point of view, because they are well suited for the study of both 3d–3d and 3d–4f competing magnetic interactions [20, 21]. Moreover, these compounds are also interesting for applications in diverse technological fields including hard and soft magnets or magnetic refrigeration [22–26]. One subset of this family are the Fe-rich R_2Fe_{17} compounds, which crystallize in the rhombohedral Th_2Zn_{17}-type structure (space group $R\bar{3}m$) for the light rare earths, with four different crystallographic sites for the iron atoms, (6c, 9d, 18f and 18h in Wyckoff notation) and a unique 6c site for the rare earth [27–29]. The binary R_2Fe_{17} compounds with R = Pr or Nd are collinear ferromagnets with Curie temperatures, T_C, around room temperature (285 ± 5 and 335 ± 5 K respectively [25, 30–32]) and relatively high values ($\mu_{Fe} \approx 2\ \mu_B$) for the Fe magnetic moments [18–20, 30].

In this paper, and through the combination of x-ray and neutron powder diffraction with electron microscopy and magnetic measurements, we show the effect of HEBM on the morphology of Nd_2Fe_{17} powders, and how mechanically induced changes in the microstructure affect their magnetic behaviour and in particular the magneto-caloric effect (MCE).

2. Experimental methods and data analysis

As starting materials for preparing Nd_2Fe_{17}, as-cast pellets pieces of commercial (Goodfellow) pure elements (Fe 99.9% and Nd 99.98%, relative to the rare earth metal content [33]) were used. Pellets of around 2 g were prepared by arc melting under a controlled Ar atmosphere, followed by a homogenization annealing lasting one week at 1373 K in order to reach a single phase with a Th_2Zn_{17}-type structure (each pellet was wrapped in a tantalum foil and sealed under vacuum in a quartz ampoule to avoid oxidation). After annealing, the pellets were directly quenched in water. The milling was performed in a high-energy planetary ball mill (Retsch PM/400) using stainless steel vials and balls. Sieved powders of Nd_2Fe_{17} (maximum diameter of 106 μm), obtained by manual pulverization of the pellets, were sealed in the vials under an Ar atmosphere (see [34] for additional details) and milled for 10 or 20 h. From here onwards the samples will be labelled 'bulk', 'BM-10 h' and 'BM-20 h' Nd_2Fe_{17} for the bulk, the 10 h and the 20 h ball milled materials, respectively. Energy dispersive x-ray spectroscopy (EDS) was used for the analysis of the elemental distribution and composition of the powders. No remarkable deviation from the starting 2:17 stoichiometry was observed in the samples.

The powder morphology at the micrometre length scale and the statistical distribution of the nanocrystalline size have been visualized and evaluated from scanning (SEM) and transmission (TEM) electron microscopy images. The crystal structure of the samples was studied at room temperature by means of x-ray (XRPD) and neutron (NPD) powder diffraction. XRPD patterns in a *d-spacing* range between 0.8 and 3.4 Å (between 25° and 150° in 2θ with $\Delta\theta = 0.02°$, and counting times of 20 s per point) were collected in high-resolution mode (Seifert model XRD3000) using graphite-monochromated Cu Kα radiation ($\lambda = 1.5418$ Å). NPD experiments were carried out at the high-flux D1B two-axis diffractometer (ILL, Grenoble, France). The diffraction patterns were collected in a *d-spacing* range between 1.65 and 7.3 Å (between 20° and 100° in 2θ with $\Delta\theta = 0.2°$, and counting times of 1 h per pattern) using a neutron wavelength of $\lambda = 2.52$ Å selected from a pyrolytic graphite (002) monochromator. For each sample approximately 4 g in mass were introduced to a vanadium cylindrical sample-holder. The full-profile refinement of the patterns has been performed using the Fullprof suite package [35], based on the Rietveld method.

The temperature and applied magnetic field dependencies of the magnetization were measured in a vibrating sample magnetometer (Lakeshore VSM 7407). Around 45 isothermal magnetization versus applied magnetic field curves, $M(H)$, were measured in the temperature range 85–420 K, with ΔT steps of 10 or 5 K for temperatures far from or near to T_C, respectively. For each $M(H)$ curve the applied magnetic field was increased from 0 to a 15 kOe with field steps of 50, 100 or 250 Oe, thus measuring around 100 points per curve. The magnetic entropy change, $|\Delta S_M|$, was determined as a function of the temperature and the applied magnetic field through the numerical integration of the isothermally measured $M(H)$ curves. For an isothermal process, ΔS_M can be evaluated by integrating the following Maxwell relation [36]:

$$\Delta S_M(T, H) = S_M(T, H) - S_M(T, 0) = \int_0^H \left(\frac{\partial M}{\partial T}\right)_H \mathrm{d}H$$

where $S_M(T, H)$ and $S_M(T, 0)$ are the magnetic entropy under an applied magnetic field H and in the absence of the magnetic field, respectively, at a fixed temperature T. The calculation of ΔS_M at a given temperature is made by a numerical integration of two consecutive $M(H)$ isotherms around such a temperature followed by the numerical derivative with temperature.

3. Results and discussion

3.1. Powder morphology, microstructure and crystal structure

The SEM images displayed in figure 1 show very different morphologies at the micrometre length scale. While the sieved powders of the bulk sample exhibit a superposition of well-defined flaky sheets with sharp edges (see figure 1(a)), both BM-10 h and BM-20 h powders look like agglomerated micron size grains (0.5–10 μm) with irregular shapes and rounded borders (see figures 1(b) and (c)) due to the severe mechanical stressing procedure. However, a higher magnification is needed to appreciate the average size of the smaller particles forming the micrometre-sized grains. In figure 1(d) (inset) we show a TEM image, corresponding to the BM-20 h sample, where distinct particles within the nanometre length scale can be resolved. The histogram describing the mean particle size distribution over a large number of individual entities (>500) follows rather well a log-normal function (figure 1(d)), giving an average size for these nanocrystallites, $\langle\tau\rangle_{TEM} = 8(1)$ nm, with a standard deviation $\sigma = 3(1)$ nm for the BM-20 h powders. An average size of 17(1) nm with $\sigma = 4(1)$ nm, is calculated from the fit corresponding to the mean particle size distribution obtained from TEM images of the BM-10 h

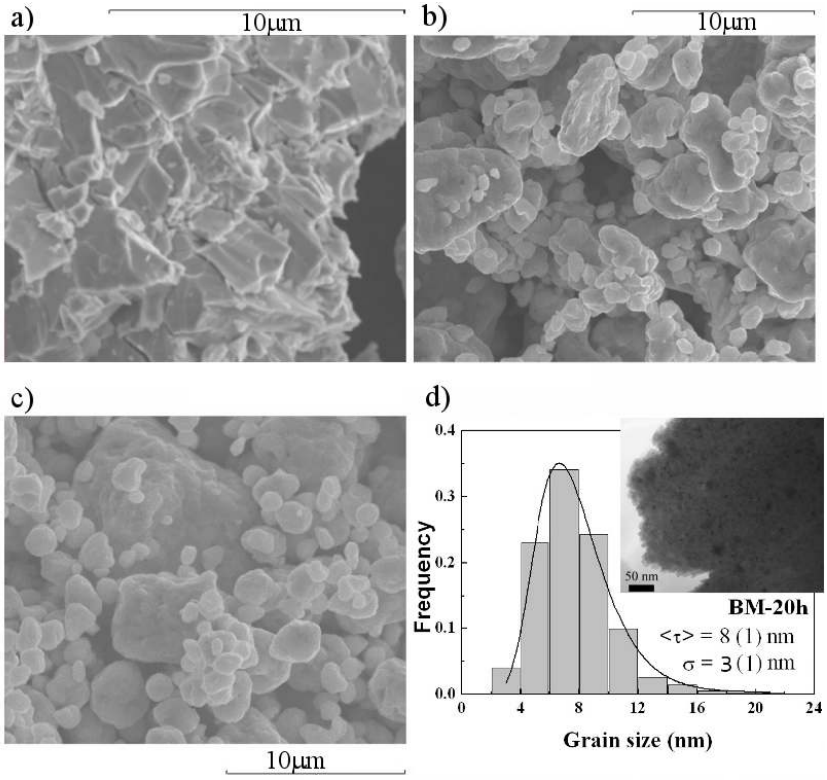

Figure 1. SEM images of bulk (a), BM-10 h (b) and BM-20 h (c) powders. (d) Particle size histogram and the fit (solid line) to a log-normal distribution, corresponding to the BM-20 h sample. The inset shows a typical TEM image.

sample. Hence, an increase of the milling time gives rise to further grain fracturing and to a considerable reduction in the nanocrystallite size.

In figure 2, the room temperature x-ray (left panel) and neutron (right panel) powder diffraction patterns for bulk, BM-10 h and BM-20 h Nd_2Fe_{17} samples are displayed. The patterns corresponding to the starting bulk alloy show peaks that can be indexed as the Bragg reflections belonging to the Nd_2Fe_{17} phase with $R\bar{3}m$ (#166) rhombohedral (Th_2Zn_{17}-type) crystal structure. We have obtained accurate values for the most important structural parameters associated with the atoms in the unit cell from the Rietveld refinement of the patterns. First we refined the non-structural parameters (scale factor, zero shift error and peak shape parameters for the pseudo-Voigt function), the cell parameters and a global isotropic temperature factor, B, for each atom. Then, the atomic coordinates of Nd [6c, $(00z)$] and Fe [6c, $(00z)$; 18f, $(x00)$; 18h, $(x\bar{x}z)$] were refined, those of 9d [$(\frac{1}{2}\,0\,\frac{1}{2})$] being fixed. Other attempts using [$(z\bar{z}x)$] coordinates for the 18h site crystallographic data [37] lead to similar results. Small profile differences, together with good agreement factors, were achieved from the final refinement (see figure 2). The values for the lattice parameters of the bulk sample (see table 1) are similar to those previously reported [38]. In addition, the position of the Bragg reflections in the diffraction patterns corresponding to BM-10 h and BM-20 h samples remain almost unaltered, thus indicating that the Th_2Zn_{17}-type crystal structure is maintained. The peak broadening indicates a drastic reduction of the grain size and therefore to the emergence of a considerable amount of disorder, mainly located at the increasing intergranular regions and/or grain boundaries [9, 16]. From the peak profile analysis (see [17] for more details), a mean crystalline size of $\langle\tau\rangle_{\mathrm{Diff}} =$ 24(3) and 14(5) nm for BM-10 h and BM-20 h samples, respectively, have been estimated, which are in reasonable agreement with those calculated from TEM histograms. The bulk polycrystalline sample does not show any broadening of the peaks with respect to the instrumental line width, thus indicating a minimum average grain size higher than 0.1 μm. However, the mechanically induced microstrain is very low, $\varepsilon \approx 0.04(2)\%$. The latter is a clear distinction with respect to the case of Fe or Fe–TM (TM = Cr, Ni, Cu, ...) ball milled powders in which the amount of induced microstrain can be over 1% [16, 17], hence, the milling process mainly produces a progressive breaking of the Nd_2Fe_{17} crystals down to the nanometre length scale. Additionally, small peaks corresponding to the reflections of a body centred cubic (bcc) crystal structure with a cell parameter $a \approx 2.87$ Å are detected in the diffraction patterns, which can be ascribed to α-Fe impurity. This impurity phase is around $3 \pm 2\%$ in the bulk sample while its amount increases up to around 8 ± 2 and $10 \pm 2\%$ in the BM-10 h and BM-20 h milled compounds, respectively.

It is worth noting that the contribution to the XRD peak width coming from induced strain is negligible (<0.1%). These findings suggest that the main process occurring during milling is a progressive grain breakage down to the nanometre length scale, concomitant with the emergence of structural

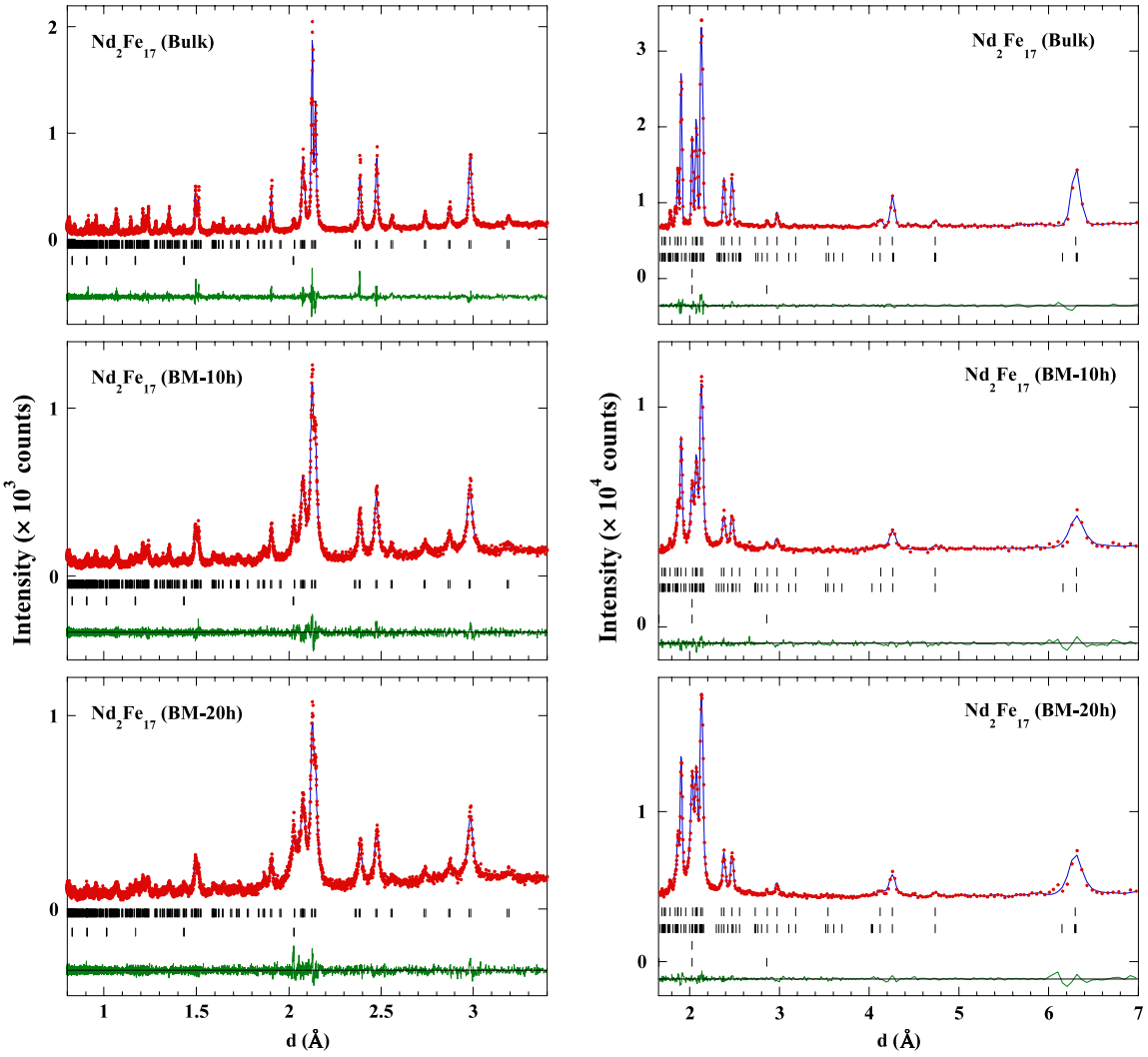

Figure 2. Observed (dots) and calculated (solid line) XRPD (left panel) and NPD (right panel) patterns for bulk, BM-10 h and BM-20 h Nd_2Fe_{17} alloys at $T = 300$ K. Positions of the Bragg reflections (in terms of the interplanar distance, d) are represented by vertical bars; the first row corresponds to the Nd_2Fe_{17} phase while the second one is associated with α-Fe impurity in the XRPD patterns. In the NPD patterns, the first two rows correspond to the Nd_2Fe_{17} phase (nuclear and magnetic) and those at the bottom are related to a α-Fe impurity (nuclear and magnetic). The observed–calculated difference is depicted at the bottom of each figure.

disorder in the material, as evidenced by the increase in the value of the Debye–Waller factor, B, (see table 1). Nevertheless, the lower resolution of the neutron diffraction pattern does not allow the estimation of reliable values for the average crystalline size and/or the induced strain. However, we have refined the nuclear as well as the magnetic structures, and the fit of the NPD patterns confirms that after the milling process the magnetic structure does not change, that is, it is still collinear ferromagnetic with parallel magnetic moments of both Nd and Fe sublattices lying along the basal plane. An accurate determination of the value of the magnetic moment, μ, in each of the five non-equivalent magnetic sites [Nd(6c), Fe1(6c), Fe2(9d), Fe3(18f) and Fe4(18h)] is not possible because there are no pure and well-separated magnetic reflections (at $T = 300$ K the expected values for μ are around 1 μ_B due to the proximity to T_C ($\approx$339 $\pm$ 5 K)), and the magnetic contribution to the intensity of the observed Bragg reflections is lower than 5%. Moreover, the broadening of these reflections due to grain size decrease adds an extra difficulty to achieve this task. In any case, the value obtained from the fit for the total magnetic moment of the Nd_2Fe_{17} phase is $\mu = 22 \pm 6$ μ_B/fu, in excellent agreement with previously reported values obtained from magnetization measurements in polycrystalline samples [39].

In table 1 the crystal unit cell parameters, atomic positions and Debye–Waller temperature factors are summarized. All these data are in reasonable agreement with previously reported data obtained from NPD on Nd_2Fe_{17} polycrystalline alloys [38]. The labelling for the Nd and Fe atomic coordinates is the same as that used in the International Tables for Crystallography [40] for the hexagonal setting of the rhombohedral space group $R\bar{3}m$ (#166).

3.2. Magnetic properties and magneto-caloric effect

Figure 3 shows the temperature and applied magnetic field dependence of magnetization for each sample. It can be seen

Table 1. Structural data (cell parameters a and c, unit cell volume, atomic positions and Debye–Waller temperature factor, B) for bulk, BM-10 h and BM-20 h Nd_2Fe_{17} ($R\bar{3}m$) compounds at $T = 300$ K obtained from the powder diffraction patterns shown in figure 2. The Bragg (R_B), profile (R_p), weighted profile (R_{wp}) and crystallographic (R_F) reliability factors are also reported (see text).

Compounds	Nd_2Fe_{17} (bulk)	Nd_2Fe_{17} (BM-10 h)	Nd_2Fe_{17} (BM-20 h)
a (Å)	8.582(1)	8.584(1)	8.582(1)
c (Å)	12.463(1)	12.463(1)	12.463(1)
V (Å^3)	795	795	795
Nd (6c)			
z	0.3448(2)	0.3440(4)	0.3427(5)
B (Å^3)	0.18(4)	1.2(1)	1.6(1)
Fe1 (6c)			
z	0.0941(4)	0.0947(6)	0.0959(8)
B (Å^3)	0.6(1)	2.1(3)	1.6(3)
Fe2 (9d)			
B (Å^3)	0.38(9)	0.8(2)	0.7(2)
Fe3 (18f)			
x	0.2873(4)	0.2876(5)	0.2861(6)
B (Å^3)	0.68(8)	1.6(2)	1.6(2)
Fe4 (18h)			
x	0.1694(3)	0.1682(4)	0.1687(5)
z	0.4899(3)	0.4912(5)	0.4894(7)
B (Å^3)	0.23(5)	1.3(1)	1.4(2)
R_B	5.8	3.4	3.4
R_p	8.5	7.6	7.6
R_{wp}	10.9	9.7	9.7
R_F	4.6	2.8	2.9
χ^2	1.3	1.1	1.1

in the low magnetic field range that while the ferromagnetic to paramagnetic transition is abrupt in the bulk sample, it becomes poorly defined as the milling time increases, starting at lower temperatures and finishing at higher temperatures than in the bulk one. The latter can be clearly observed in figure 4, where the normalized magnetization versus temperature curve in the immediate vicinity of the ferromagnetic to paramagnetic transition, measured under $H = 200$ Oe, is depicted. The value for the Curie temperature has been estimated from the minimum of the dM/dT versus T curve, using the data of figure 4. The bulk sample exhibits a sharp and well-defined minimum giving a value of $T_C = 339 \pm 5$ K, while the precise estimation of T_C is difficult for the milled samples, because the dM/dT versus T curves display broad and asymmetric minima located at around 340 ± 20 K. Therefore, a broad distribution of T_C values should be considered instead of a unique and well-defined one for the milled samples. This fact could be a direct consequence of the induced structural disorder and the slightly different local environments of the atoms at the grain boundaries, giving rise to a modification of their magnetic behaviour, as has been previously observed in other Fe-based nanostructured magnetic materials [31, 34, 41].

The saturation magnetization, M_s, at $T = 100$ K for the three samples was estimated from the fit of the $M(H)$ curves to an approach-to-saturation law:

$$M = M_s\left(1 - \frac{b}{H^2}\right) + \chi_0 H. \qquad (1)$$

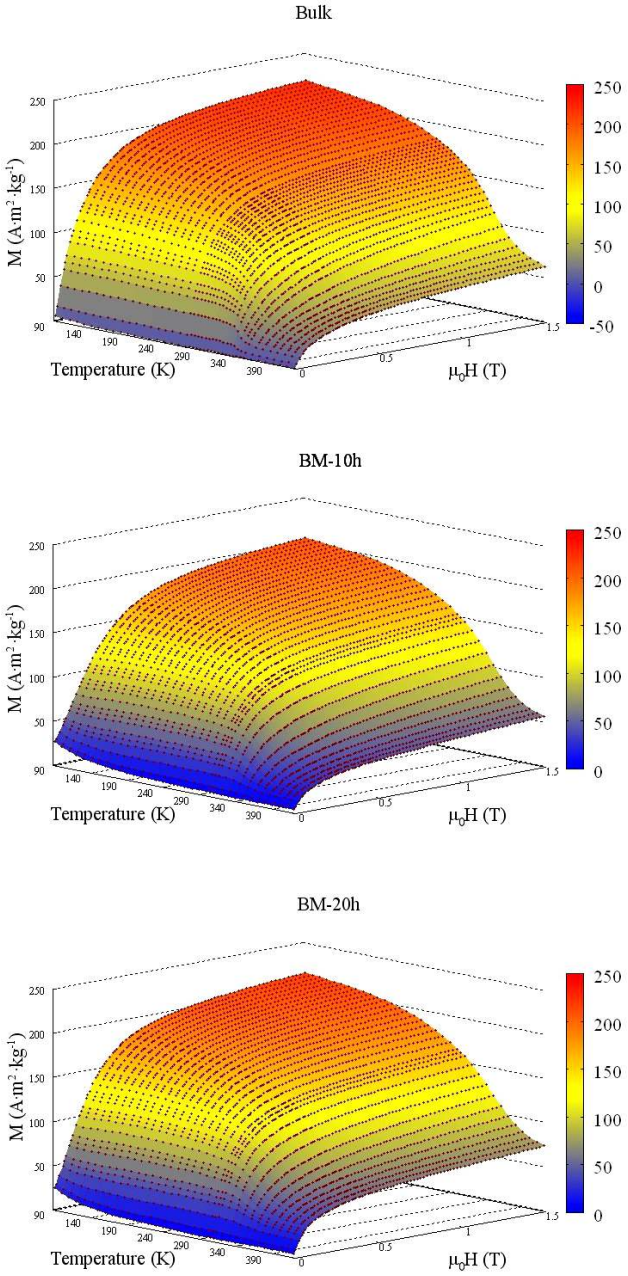

Figure 3. Temperature and applied magnetic field dependencies of the magnetization for the bulk and milled Nd_2Fe_{17} samples.

The fit gives values of 138 ± 5 A m^2 kg^{-1} (bulk), 128 ± 5 A m^2 kg^{-1} (BM-10 h) and 134 ± 5 A m^2 kg^{-1} (BM-20 h) for the M_s. However, these different values must be interpreted with care because the $M(H)$ curves corresponding to the milled samples show an increase of the magnetic anisotropy (which is reflected as a 30% increase in the values of b and χ_0 parameters, see equation (1)) and clearly the saturation regime is not reached under an applied magnetic field of 15 kOe. Moreover, both the coercivity and remanence increase in BM-10 h and BM-20 h samples with respect to those of the bulk alloy, giving rise to a non-zero magnetization value at low applied magnetic fields (see figure 3). We must point out that for every isothermal $M(H)$ curve, after measuring the last value of M ($H = 15$ kOe), H is removed

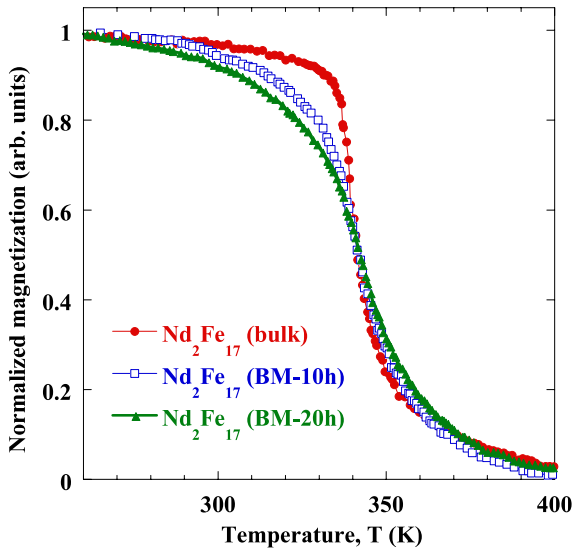

Figure 4. Temperature dependence of the magnetization (normalized to the value at $T = 260$ K) for the bulk and milled Nd_2Fe_{17} samples. Note that the contribution to the magnetization coming from the ferromagnetic α-Fe impurity has been subtracted for clarity.

and the temperature is changed to the next selected value in order to begin the measurement of the next isothermal $M(H)$ curve. In this situation, the first measured M value ($H = 50$ Oe) for each $M(H)$ isotherm is affected by the not-negligible values of coercivity and remanence of the sample. These facts have been previously observed in other milled materials [42], being a direct consequence of the increase of the magnetic anisotropy. Such magnetic anisotropy enhancement could be caused by the drastic decrease of the mean crystallite size down to the nanometre length scale, giving rise to complex magnetic interactions between the nanocrystals and/or nanograin boundaries [23, 35]. Besides that, it is observed that as the temperature is increased above the T_C of the Nd_2Fe_{17} phase, the magnetic field dependence of the magnetization does not resemble a linear trend, as could be expected for a paramagnetic system. The latter is due to both (i) the existence of the α-Fe impurity phase ($T_C = 1044$ K) contributing to the magnetization and (ii) the existence of short-range magnetic correlations that could extend even up to $T = 2T_C$.

In figure 5 a 3D view of the temperature and magnetic field dependence of the magnetic entropy change in the bulk and milled samples is depicted.

The abrupt decrease of the magnetization near T_C in the bulk alloy (see figure 3), gives rise to a remarkable change in its magnetic entropy, reaching a maximum value of $|\Delta S_M| \approx 2.6$ J kg^{-1} K^{-1} at 15 kOe (see figure 6). For both BM-10 h and BM-20 h samples the $|\Delta S_M|(T)$ curves exhibit an evident broadening, as could be expected from the slower decrease of M in this temperature range (see figures 3 and 4), the maximum value of $|\Delta S_M|$ (1.85 and 1.6 J kg^{-1} K^{-1} for BM-10 h and BM-20 h, respectively) is lower than that quoted above for the bulk sample (2.6 J kg^{-1} K^{-1}) under the same applied magnetic field. The temperature at which the maximum of $|\Delta S_M|(T)$ occurs (≈340 K) is nearly the same for the three samples and

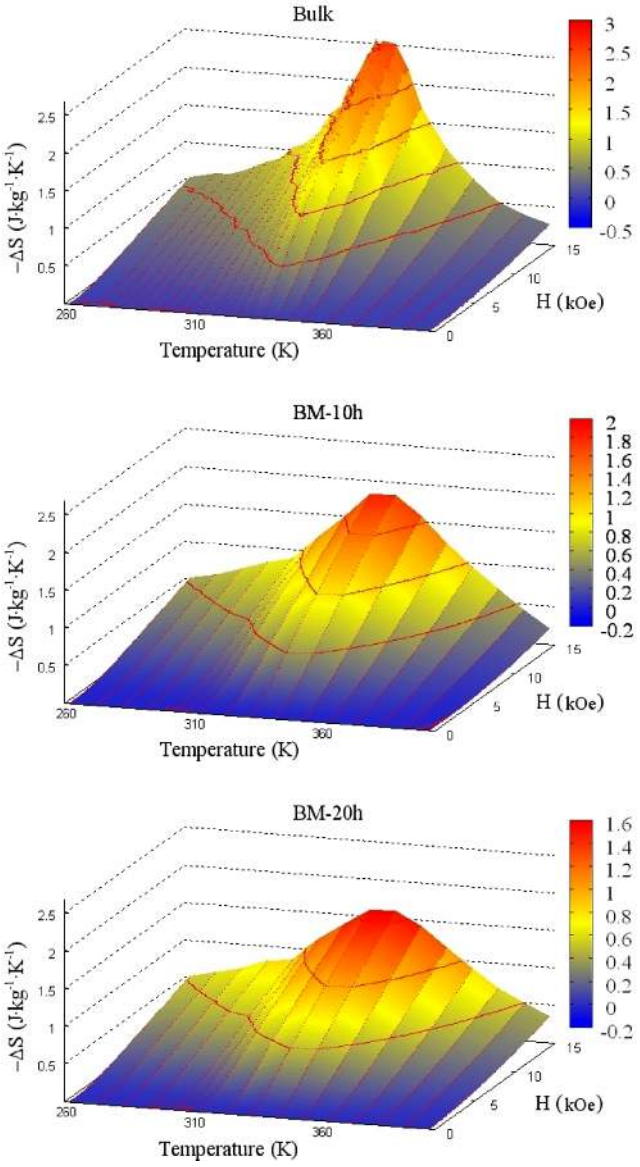

Figure 5. Temperature and applied magnetic field dependencies of the magnetic entropy change for the bulk and milled Nd_2Fe_{17} samples.

it almost coincides with the value of T_C in the bulk sample. It is also worth noting the asymmetric shape of the $|\Delta S_M|(T)$ peak exhibited by the milled sample, with a long tail after the maximum, which is undoubtedly correlated with that of the temperature dependence of magnetization.

Therefore, the ball milling process causes a decrease of the value of $|\Delta S_M|$, but at the same time, the MCE spreads out over a wider temperature range [12, 25, 26], as can be seen from the inset of figure 6, where the magnetic field dependence of the δT_{FWHM} parameter (defined as the full width at half maximum of $|\Delta S_M|(T)$ peak) is shown. The latter is an important parameter to be taken into account when the refrigerant capacity (RC) or relative cooling power (RCP) [25, 43, 44] of a material of potential interest in magnetic refrigeration has to be evaluated. An estimation of the refrigerant capacity ($RC = \delta T_{FWHM} \times |\Delta S_M|^{max}$) gives similar values for the three samples, 83, 87 and 87 J kg^{-1}

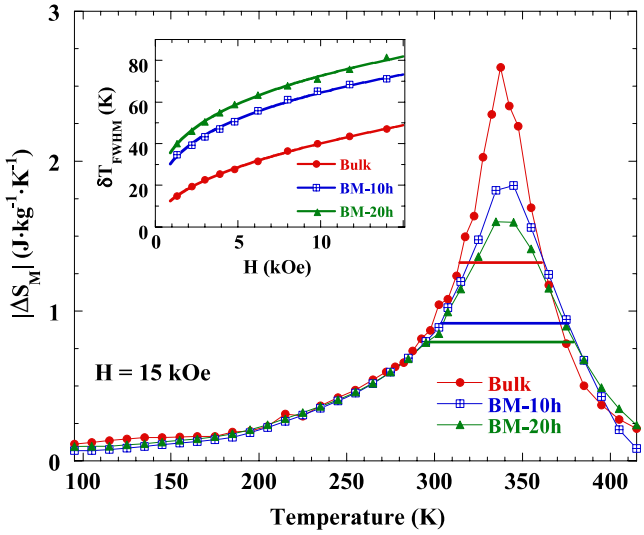

Figure 6. Temperature dependence of $|\Delta S_M|$ under $H = 15$ kOe for bulk and milled Nd_2Fe_{17} samples. The horizontal lines represent δT_{FWHM} for each sample. The inset shows the magnetic field dependence of δT_{FWHM} for all the samples (see text).

for bulk, BM-10 h and BM-20 h, respectively. Even though a slight increase (≈5%) in the value of RC is observed after milling, we cannot conclude that the mechanically induced microstructural changes improve the magneto-caloric effect in these compounds in the applied magnetic field range between 0 and 15 kOe.

4. Summary

Nanostructured Nd_2Fe_{17} powders have been obtained from the starting arc-melted massive compound by means of high-energy ball milling after milling times of 10 and 20 h. A reduction of the average crystallite size below 20 nm, with almost vanishing values for the mechanically induced microstrain ($\varepsilon < 0.1\%$) has been found. The Th_2Zn_{17}-type crystal structure, as well as the atomic positions in the unit cell, remain unaltered, thus suggesting a modification of the microstructure mainly due to progressive grain fracturing. The severe mechanical processing of the samples generates a high degree of disorder that should be mainly located at the grain boundaries, thus affecting the magnetic behaviour in two important aspects: (i) applied magnetic fields much higher than 15 kOe are needed to saturate the samples due to the increase of magnetic anisotropy; and (ii) the magnetization versus temperature curve shows a slow decrease around room temperature in the mechanically stressed sample, suggesting that the nanostructured powders do not have a unique and well-defined value of T_C. The latter gives rise to a reduction in the maximum value of the magnetic entropy change together with the broadening of the $|\Delta S_M|(T)$.

Acknowledgments

Financial support from FEDER and Spanish MICINN (Projects Nos MAT2008-06542-C04-03, MAT2007-65227 & NAN2004-09203-C04-03) and from the PAI of the Regional Government of Andalucia (Project No. P06-FQM-01823) is acknowledged. We thank ILL and CRG-D1B for allocating neutron beam time. PA and JSM are grateful for their research contracts to FICyT and MICINN respectively. The SCTs at the University of Oviedo are also acknowledged.

References

[1] Suryanarayana C 2001 *Prog. Mater. Sci.* **46** 1
[2] Zhang D L 2004 *Prog. Mater. Sci.* **49** 537
[3] Ma E 2005 *Prog. Mater. Sci.* **50** 413
[4] Randrianantoandro N, Cooper R J, Greneche J M and Cowlam N 2002 *J. Phys.: Condens. Matter* **14** 9713
[5] Mishra D, Srinivasan A and Perumal A 2008 *J. Phys. D: Appl. Phys.* **41** 215003
[6] Gorria P, Garitaonandia J S, Pérez M J, Blanco J A and Campo J 2009 *Phys. Status Solidi (RRL)* **3** 28
[7] Mishra D, Perumal A and Srinivasan A 2009 *J. Appl. Phys.* **105** 07A306
[8] Gorria P, Martinez-Blanco D, Blanco J A, Hernando A, Garitaonandia J S, Férnandez Barquín L, Campo J and Smith R I 2004 *Phys. Rev.* B **69** 214421
[9] Gorria P, Martinez-Blanco D, Pérez M J, Blanco J A and Smith R I 2005 *J. Magn. Magn. Mater.* **294** 159
[10] Valderruten J F, Pérez Alcázar G A and Grenèche J M 2008 *J. Phys.: Condens. Matter* **20** 485204
[11] Gorria P, Martinez-Blanco D, Blanco J A, Pérez M J, Hernando A, Férnandez Barquín L and Smith R I 2005 *Phys. Rev.* B **72** 014401
[12] Ipus J J, Blázquez J S, Franco V, Conde A and Kiss L F 2009 *J. Appl. Phys.* **105** 123922
[13] Gorria P *et al* 2009 *Phys. Status Solidi (RRL)* **3** 115
[14] Kalita M P C, Perumal A and Srinivasan A 2009 *J. Phys. D: Appl. Phys.* **42** 105001
[15] Gorria P *et al* 2009 *Phys. Rev.* B **80** 064421
[16] Martinez-Blanco D, Gorria P, Pérez M J, Blanco J A and Smith R I 2007 *J. Magn. Magn. Mater.* **316** 328
[17] Martinez-Blanco D, Gorria P, Blanco J A, Pérez M J and Campo J 2008 *J. Phys.: Condens. Matter* **20** 335213
[18] Buschow K H J 1977 *Rep. Prog. Phys.* 1977 **40** 1179
[19] Buschow K H J 1980 *Ferromagnetic Materials* vol 1, ed E P Wohlfarth (Amsterdam: North-Holland) p 297
[20] Givord D and Lemaire R 1974 *IEEE Trans. Magn.* **10** 109
[21] Piqué C, Blanco J A, Burriel R, Abad E, Artigas M and Fernández-D íaz M T 2007 *Phys. Rev.* B **75** 224424
[22] Hadjipanayis G C 1999 *J. Magn. Magn. Mater.* **200** 373
[23] Skomski R and Coey J M D 1993 *Phys. Rev.* B **48** 15812
[24] Gschneidner K A Jr, Pecharsky V K and Tsokol A O 2005 *Rep. Prog. Phys.* **68** 1479
[25] Gorria P, Sánchez Llamazares J L, Álvarez P, Pérez M J, Sánchez Marcos J and Blanco J A 2008 *J. Phys. D: Appl. Phys.* **41** 192003
[26] Sánchez Llamazares J L, Pérez M J, Álvarez P, Santos J D, Sánchez M L, Hernando B, Blanco J A, Sánchez Marcos J and Gorria P 2009 *J. Alloys Compounds* **483** 682
[27] Ray A E 1966 *Acta Crystallogr.* **21** 426
[28] Johnson Q, Wood D H and Smith G S 1968 *Acta Crystallogr.* B **24** 274
[29] Johnson Q, Smith G S and Wood D H 1969 *Acta Crystallogr.* B **25** 464
[30] Weitzer F, Hiebl K and Rogl P J 1989 *J. Appl. Phys.* **65** 4963
[31] Álvarez P, Sánchez Llamazares J L, Pérez M L, Hernando B, Santos J D, Sánchez-Marcos J, Blanco J A and Gorria P 2008 *J. Non-Cryst. Solids* **354** 5172
[32] Franse J J M and Radwanski R J 1993 *Handbook of Magnetic Materials* vol 7, ed K H J Buschow (Amsterdam: Elsevier) p 307

[33] Gschneidner K A Jr 1993 *J. Alloys Compounds* **193** 1
[34] Gorria P, Álvarez P, Sánchez Marcos J, Sánchez Llamazares J L, Pérez M J and Blanco J A 2009 *Acta Mater.* **57** 1724
[35] Rodríguez Carvajal J 1993 *Physica* B **192** 55
[36] Tishin A M and Spichkin Y I 2003 *The Magnetocaloric Effect and its Applications* (Bristol: Institute of Physics Publishing)
[37] Girt E, Altounian Z, Swainson I P, Krishnan K M and Thomas G 1999 *J. Appl. Phys.* **85** 4669
[38] Long G J, Marasinghe G K, Mishra S, Pringle O A, Hu Z, Yelon W B, Middleton D P, Buschow K H J and Grandjean F 1994 *J. Appl. Phys.* **76** 5383
[39] Girt E, Guillot M, Swainson I P, Krishnan K M, Altounian Z and Thomas G 2000 *J. Appl. Phys.* **87** 5323
[40] International Tables for Crystallography 2002 *Space-Group Symmetry* vol A, ed T Hahn (Dordrecht: Kluwer)
[41] Hernando A, Navarro I and Gorria P 1995 *Phys. Rev.* B **51** 3281
[42] Blázquez J S, Franco V, Conde A and Roth S 2006 *Phil. Mag.* **86** 2271
[43] Franco V, Borrego J M, Conde A and Roth S 2006 *Appl. Phys. Lett.* **88** 132509
[44] Franco V, Conde C F, Conde A and Kiss L F 2007 *Appl. Phys. Lett.* **90** 052509